Coalescence-induced nanodroplet jumping

Hyeongyun Cha, Chenyu Xu, Jesus Sotelo, Jae Min Chun, Yukihiro Yokoyama, Ryan Enright, and Nenad Miljkovic

Coalescence-Induced Nanodroplet Jumping

Hyeongyun Cha[1,3], Chenyu Xu[1], Jesus Sotelo[1], Jae Min Chun[1], Yukihiro Yokoyama[1], Ryan Enright[2], and Nenad Miljkovic[1,3],*

[1]*Department of Mechanical Science and Engineering, University of Illinois Urbana, Illinois 61801, USA*

[2]*Thermal Management Research Group, Efficient Energy Transfer (ηET) Department, Bell Laboratories Ireland, Nokia, Blanchardstown Business & Technology Park, Snugborough Road. Dublin 15, Ireland*

[3]*International Institute for Carbon Neutral Energy Research (WPI-I2CNER), Kyushu University, 744 Moto-oka, Nishi-ku, Fukuoka 819-0395, Japan*

*Corresponding Author E-mail: nmiljkov@illinois.edu

Abstract:

Water vapor condensation on superhydrophobic surfaces has received much attention in recent years due to the ability of such surfaces to shed microscale water droplets via coalescence-induced droplet jumping, resulting in heat transfer, anti-icing, and self-cleaning performance enhancement. Here, we report for the first time the coalescence-induced removal of water nanodroplets ($R \approx 500$ nm) from superhydrophobic carbon nanotube (CNT) surfaces. The two-droplet coalescence time is measured for varying droplet Ohnesorge numbers, confirming that coalescence prior to jumping is governed by capillary-inertial dynamics. By varying the conformal hydrophobic coating thickness on the CNT surface, the minimum jumping droplet radius was shown to increase with increasing solid fraction and decreasing apparent advancing contact angle, allowing us to explore both hydrodynamic limitations stemming from viscous dissipation and surface adhesion limitations. We find that, even for the smallest nanostructure length scale (≤ 100 nm) and lowest surface adhesions, non-ideal surface interactions and the evolved droplet morphology play defining roles in limiting the minimum size for jumping on real surfaces. The outcomes of this work demonstrate the ability to passively shed nanometric water droplets, which has the potential to further increase the efficiency of systems that can harness jumping droplets for a wide range of energy and water applications.

Keywords: jumping-droplet, coalescence, condensation, nanodroplet, heat transfer

I. INTRODUCTION

Water vapor condensation is routinely observed in nature and has a large influence on the performance of industrial systems [1-5]. When water condenses on non-wetting hydrophobic surfaces, it undergoes 'dropwise' condensation [6] with an order of magnitude enhanced heat transfer under pure vapor conditions when compared to condensation on wetting hydrophilic substrates due to the formation of small liquid droplets which grow, shed *via* gravitational body force (≈ 2 mm for water) and, in the process, clear the surface for re-nucleation [7]. More recently, researchers have discovered that microdroplets (~10-100 µm) condensing and coalescing on suitably designed superhydrophobic surfaces can lead to droplets jumping away from the surface irrespective of gravity due to surface-to-kinetic energy transfer [8-13]. This spontaneous droplet removal [14-24] has been utilized for a variety of applications including self-cleaning [25-27], thermal diodes [28], anti-icing [29-32], vapor chambers [33], electrostatic energy harvesting [34-36], fiber-based coalescers [37], and condensation heat transfer enhancement [38-55]. The minimum droplet size where coalescence-induced jumping occurs governs the performance of applications exploiting the phenomenon. Removal of the condensate at smaller length scales reduces the thermal transport resistance through the condensate [40], enhances jumping speeds due to more efficient surface-to-kinetic energy transfer [9], and allows for the more efficient control of droplet motion with external fields against adverse forces such as gravity or vapor flow [51]. However, the mechanism governing the minimum jumping droplet size is not well understood. While a number of previous studies have reported that below a critical radius of ≈10 µm (at standard laboratory conditions) coalescing water droplets on superhydrophobic surfaces do not jump due to hydrodynamic limits stemming from internal viscous dissipation during coalescence [17,49,56-61], recent experimental and numerical

3

evidence indicate that a smaller range of jumping droplet sizes (< 10 µm) should be possible [9-11,62]. Here, we report, for the first time, direct experimental evidence of water nanodroplet jumping on ultra-low adhesion carbon nanotube (CNT) surfaces. Through theoretical and experimental analysis of two-droplet coalescence timescales during jumping, we show that inertial-capillary dynamics govern jumping down to nanodroplet length scales ($R \approx 500$ nm) before viscous effects become dominant. Previous findings are reconciled by realizing that the combined effects of adhesion, contact angle hysteresis, and initial wetting behavior governed by the surface structure morphology and length-scale, define the minimum droplet departure size and observed speed reduction at low radii. The insights gained from this study have implications for enhancing the efficiency and performance of a wide array of energy and water applications.

II. EXPERIMENTS

The growth, coalescence, and jumping of droplets were studied using a custom built top-view optical light microscopy set-up by condensing water vapor either from the ambient, or from a saturated vapor supply on substrates having temperatures $T_w = 1 \pm 0.5$°C. A description of the experimental setup with procedures is detailed in the Supplemental Material, Section S.2 [63]. A CNT coated silicon wafer was chosen as a model condensation substrate due to the small length scale of the nanotubes (~10 nm), the low solid fraction (φ) of the short nanotubes and, thus, the potential for achieving ultra-low adhesion after hydrophobic functionalization. Carbon nanotubes were grown by chemical vapor deposition (CVD) on silicon with the procedures detailed in Ref. [9]. The thermally grown CNTs had a typical outer diameter of $d \approx 7$ nm and formed tangled turf instead of an aligned forest due to the short growth time (≈ 5 minutes). The characteristic turf height was determined to be $h \approx 1 \pm 0.3$ µm via atomic force microscopy. To functionalize the

surfaces, a proprietary fluorinated polymer was deposited using plasma enhanced vapor deposition (P2i) under low pressure at room temperature. This process allows for the development of a highly conformal, but thin (≈10 nm) polymer layer (Fig. 1a, b). Note, P2i polymer deposition was chosen as the method of hydrophobic functionalization due to the ability to accurately control the thickness of the coating (± 5 nm) and the inability to conformally coat the pristine CNTs with a thinner (~1 nm) self-assembled-monolayer (SAM). Furthermore, polymer functionalization offers a more durable hydrophobic coating when compared to many SAM chemistries [38], resulting in improved sample robustness. Goniometric measurements (MCA-3, Kyowa Interface Science Ltd.) of droplets on a smooth P2i coated silicon wafer showed advancing and receding contact angles of $\theta_a = 124.3 \pm 3.1°$ and $\theta_r = 112.6 \pm 2.8°$, respectively. To quantify the effects of droplet-surface interaction, we also fabricated identical CNT turf samples to the one described above (CNT1), but with varying fluoropolymer thicknesses of ≈30 nm (CNT2, Fig. 1c), 60 nm (CNT3, Fig. 1d), and 90 nm (CNT4, Fig. 1e) to vary the effective solid fraction and, thus, the surface adhesion characteristics. Using the values of the advancing angles on the rough and smooth P2i surfaces, we estimated the solid fraction of the 10, 30, 60, and 90 nm CNT surfaces to be $\varphi = (\cos\theta_a^{app} + 1)/(\cos\theta_a + 1) \approx 0.017$, 0.06, 0.15, and 0.23, respectively. The CNT2, CNT3, and CNT4 samples had an increased effective solid fraction due to the filling of nanoscale gaps between CNTs (Figs. 1c-d), resulting in a reduced apparent contact angle (θ_a^{app}), increased droplet-surface adhesion and increased contact angle hysteresis. The apparent advancing and receding contact angles ($\theta_a^{app}/\theta_r^{app}$) on the CNT1, CNT2, CNT3, and CNT4 surfaces were measured to be ≈ 173°/164°, 163°/152°, 159°/146°, and 154°/140°, respectively.

III. MINUMUM JUMPING DROPLET SIZE

Droplet nucleation on the CNT surfaces occurred primarily within nanostructures (due to small φ) in a spatially random fashion [64] and, while growing beyond the confines of the structures, the apparent contact angle increased as the droplets developed a balloon-like shape with a liquid bridge at the base [41,64]. On the CNT1 surface, once droplets grew to diameters large enough to coalesce with neighboring droplets ($R \approx 5$ μm for ambient conditions), frequent out-of-plane jumping was observed. Due to the high conformality and low defect density of the P2i coating, condensation experiments in ambient conditions with $T_{air} = 22 \pm 0.5$°C and relative humidity $\Phi = 28 \pm 1\%$ resulted in nucleation densities of $N \leq 2.5$ x 10^9 droplets/m^2. In order to study the behavior of interacting *nanoscale* droplets, the nucleation density on the CNT1 surface was elevated by increasing the saturation temperature of the incoming vapor supply to $T_{air} = 35 \pm 0.5$°C and relative humidity $\Phi \approx 100 \pm 1\%$. The increased saturation temperature resulted in a supersaturation ($S = [\Phi P_{sat}(T_{air})]/P_{sat}(T_w)$) increase from $S = 1.02 \pm 0.035$ to $S = 8.56 \pm 0.4$, and a corresponding increase in the nucleation rate and active nucleation site density to $N \geq 1.1$ x 10^{10} droplets/m^2, consistent with nucleation site activation [65]. At the elevated nucleation densities, the center-to-center spacing between neighboring droplets was as low as ≈ 500 nm. Surprisingly, frequent out-of-plane jumping was still observed at these reduced droplet coalescence length scales on the CNT1 surface (Fig. 2), with droplets having radii as small as $R_1 = 533 \pm 75$ nm and $R_2 = 792 \pm 75$ nm coalescing and jumping from the surface (Fig. 2b). In addition to jumping resulting from the coalescence of two nanodroplets (defined as nano based on their radii), serial coalescence between three nanodroplets resulted in jumping as well (Fig. 2c, d). Conservation of mass of the coalescing droplets showed droplet departure radii as

6

small as $R_j = 700 \pm 75$ nm, well below the previously observed limit of $R_j > 5$ μm. It is important

to note that the higher supersaturations used in these experiments ($S = 8.56 \pm 0.4$) did not lead to

nucleation-mediated surface flooding, which was shown to occur for $S > 1.12$ for nanostructured

superhydrophobic copper oxide (CuO) surfaces [50]. Increased supersaturations without flooding

were achieved as a result of the reduction in structure length scale from $l \approx 1$ μm (CuO) to $l \approx 50$

- 100 nm (CNT1) and the characteristically lower nucleation density on the P2i coating at a given

supersaturation. The reduced length scale allowed for the average spacing between randomly

distributed nucleation sites ($\langle L \rangle$) to be much smaller while simultaneously allowing individual

droplets to form the energetically favorable partially wetting droplet morphology prior to

coalescence and jumping ($\langle L \rangle / l \gg 1$) [38,39,50,64]. Furthermore, the nanoscale droplet jumping

phenomena was not observed on the CNT2, CNT3, or CNT4 surfaces, which, as we will discuss

later, can be attributed to increased droplet-surface adhesion.

IV. COALESCENCE TIMESCALE

To explain the jumping of nanoscale droplets observed here, we begin by examining the

hydrodynamics of droplet coalescence between two equally sized droplets on the

superhydrophobic CNT surfaces. Immediately after the interfaces of the two droplets touch, a

radially accelerating liquid bridge develops due to the curvature difference between the bridge

radius ($1/r_b$) and the radii of the coalescing droplets ($1/R$). The momentum of this radial flow

structure has been shown to drive droplet jumping [22]. For the droplet length scales considered

here (500 nm < R < 200 μm), the Ohnesorge number, $Oh = \mu/(\rho\gamma R)^{1/2}$, where μ (=1.73 mPa·s),

ρ (=999.85 kg/m³), and γ (=75.5 mN/m) are, respectively, the water dynamic viscosity, density,

and surface tension, corresponds to $0.26 > Oh > 0.013$. For $Oh < 1$, droplet coalescence occurs in

two distinct regimes [66,67]. When $r_b/R < $ Oh, droplets undergo coalescence in the inertially-limited viscous regime where growth of the bridge radius is governed by a balance between viscous, inertial, and surface tension forces, $r_{b,v} = \gamma t/\mu$. As the liquid bridge proceeds to grow, and reaches $r_b/R > $ Oh, the droplets enter the inertially-limited regime where growth of the bridge radius is governed by a balance between inertia and surface tension forces, $r_{b,i} = D_0(\gamma R/\rho)^{1/4}t^{1/2}$, where D_0 is a constant with value ranging between 1.39 and 1.62 [66,68,69]. The crossover between these two regimes occurs when the Reynolds number (Re $= \rho UL/\mu$) based on the neck height ($L = r_b^2/2R$) approaches unity (Re ≈ 1), corresponding to a critical bridge radius of $r_c \approx 8\mu(R/\rho\gamma D_0^4)^{1/2}$ [66]. For the smallest droplets coalescing on our CNT surfaces ($R \approx 500$ nm), $r_c = 398$ nm based on $D_0 = 1.62$, which is below the observed minimum jumping radius for CNT1. For larger droplets, the discrepancy is even greater, showing $r_c/R = 0.33$ for $R = 3$ μm, and $r_c/R = 0.18$ for $R = 10$ μm. The early crossover between the two regimes ($r_c/R \ll 1$) indicates that inertial-capillary effects dominate the coalescence hydrodynamics with viscosity playing a limited role for microscale water droplets ($R > 1$ μm). Indeed, by calculating the viscous-to-inertial crossover time, $\tau_c = 64\mu^2[R/(\rho\gamma^3 D_0^{12})]^{1/2}$, and normalizing it to the total coalescence time for the bridge radius to reach the droplet radius ($r_b = R$), $\tau_{tot} = \tau_v + \tau_i = r_c\mu/\gamma + (\rho/\gamma D_0^4)^{1/2}(R^{3/2} - r_c^{3/2})$, we can estimate the time spent in each regime during coalescence. For droplets having radii $R = 0.5, 3$, and 10 μm, we obtain $\tau_c/\tau_{tot} = 0.65, 0.1$, and 0.029, respectively, indicating that inertial-capillary forces govern droplet coalescence even at nanometric length scales. Therefore, the underlying cause preventing droplet jumping for $R > 1$ μm at standard laboratory conditions is not viscous dissipation (as put forward in Refs. [17,49,56-61]), but most likely a droplet-surface interaction mechanism arising due to finite surface adhesion and the evolving droplet morphology at length scales comparable to that of the

surface structures. Note, the minimum coalescing droplet size reported here ($R \approx 556$ nm) that leads to jumping agrees well with the theory, as the crossover radius approaches the coalescence radius at these small length scales ($r_c = 420$ nm). Observation of ultra-small droplets coalescing ($R < 500$ nm) was difficult to observe due to the resolution limitations of our optical microscopy setup (diffraction limit). However, coalescence without jumping on our CNT1 surface was observed for droplets having sizes as small as $R_1 = R_2 = 375 \pm 300$ nm due to a combination of viscous effects and an inability to further decrease surface adhesion of our CNT1 surface.

To verify that the coalescence hydrodynamics are indeed dominated by inertial effects for the droplet size range discussed above, we experimentally measured the coalescence timescale (τ_{tot}) for a variety of droplet Oh ($0.1 > $ Oh > 0.013, corresponding to 3 μm $< R <$ 200 μm). We were unable to characterize smaller droplets ($R < 3$ μm) due to the exceedingly fast ($\tau_{tot} < 1$ μs) coalescence process at these length scales and the limitation of our high-speed camera to 10^6 frames per second. Individual coalescence events were observed *via* top-down high speed imaging of condensing water vapor from standard laboratory conditions (Fig. 3a). To measure the coalescence time of both jumping and non-jumping events, we tested the CNT1 and CNT3 samples. While the CNT1 sample showed droplet jumping for all droplet length scales (500 nm $<$ $R <$ 200 μm), many coalescence events on the CNT3 surface resulted in non-jumping due to increased adhesion. Figure 3(b) demonstrates that droplet jumping hydrodynamics on the superhydrophobic CNT surfaces are indeed governed by inertial effects down to the smallest droplet sizes we could measure. The jumping and non-jumping experimental data is in good agreement with the predicted value from the inertial regime ($\tau_i = (R^3\rho/\gamma D_0{}^4)^{1/2}$) and a poor fit with the inertially-limited viscous regime ($\tau_v = R\mu/\gamma$). Furthermore, the experimental data reveals no statistical difference between the coalescence timescale of jumping and non-jumping

events. These findings support the view that a surface interaction mechanism rather than a fundamental hydrodynamic limitation governs the minimum droplet jumping size over the range of Oh investigated. Furthermore, the previously reported lower than expected jumping speeds cannot be attributed to viscous effects during coalescence [17,49,56-61], as the jumping speeds in previous works decrease faster than observed in experiments on similar CNT surfaces shown here in this range of Oh (< 0.1) [9], pointing to a non-hydrodynamic mechanism [9-11,62].

V. DROPLET-SURFACE INTERACTION

To quantify the effects of droplet-surface interaction, we experimentally observed the condensation behavior on the CNT2, CNT3, and CNT4 surfaces. As $\theta_a^{app}/\theta_r^{app}$ decreased from $\approx$ 173º/164° (CNT1), to 163º/152° (CNT2), 159º/146° (CNT3), and 154º/140° (CNT4), the minimum droplet departure radius increased correspondingly to R_j ($\approx 2^{1/3}R$) $\approx$ 700 nm, 4.5 µm, 20 µm, and no jumping, respectively.

To estimate the excess surface energy required to overcome the work of adhesion associated with finite surface adhesion, we developed an analytical model that considers the coalescence of two droplets having center-to-center spacing $2R$, with partially pinned liquid regions underneath each droplet characterized by a radius, r_p. No jumping will occur if the available excess liquid/vapor surface energy released during coalescence is unable to overcome the work of adhesion associated with the finite wetted area of the droplets on the surface. The work of adhesion is considered to play a role throughout the coalescence process, from the initial stage of bridge formation (identified as stage 1 & 2 by Liu et al. [10]) to the acceleration of the droplet mass perpendicular to the surface (identified as stage 3 by Liu et al. [10]). Recent 3D simulations of the coalescence process on surfaces with θ < 180° have provided useful

10

qualitative information regarding the characteristic surface wetting behavior of jumping droplets at the different stages of coalescence [13]. To develop our model incorporating the role of surface adhesion on droplet jumping within a simple energy balance framework, we divide the jumping process into three states rather than the two states typically considered [17,57,58,70]. Specifically, in addition to the initial state before coalescence (E_1) and the final jumping state (E_3), we consider an intermediate state representing the coalesced droplet on the surface prior to departure (E_2) as shown in Fig. 4. We note that this intermediate state (E_2) is a well-defined equilibrium state if jumping does not occur.

The excess liquid-vapor interfacial energy driving the jumping process, $\Delta E_{31,lv}$, is calculated between the initial (E_1) and final energy state (E_3), albeit corrected by an efficiency term, η, that captures the characteristic incomplete conversion of excess liquid-vapor interface energy to the translational kinetic energy of the jumping droplet and viscous effects [9,10]. Furthermore, we also account for the difference in the work of adhesion between E_1 and E_2, $W_{31} - W_{32}$, where W_{32} is characteristically smaller than W_{31}. We consider this adhesion term balancing directly against the **total** excess energy, i.e., $\Delta E_{31,lv} + (W_{31} - W_{32})$, since the work of adhesion to be overcome is acting against droplet mass moving parallel to the surface as the radial flow, characteristic of the coalescence process, begins to develop. Finally, in order to transition from E_2 to E_3, the droplet needs to overcome the work of adhesion associated with the droplet base area in state E_2 (W_{32}), and balances directly against the **available** excess energy for jumping, i.e., $\eta[\Delta E_{31,lv} + (W_{31} - W_{32})]$. Thus, in the ideal limit of zero contact angle hysteresis, we estimate the energy available for jumping as

$$E_j \approx \eta[\Delta E_{31,lv} + (W_{31} - W_{32})] + W_{32}\,,$$

(1)

where the excess liquid-vapor interface energy between state E_3 and E_1 is given by

$$\Delta E_{31,\mathrm{lv}} = \gamma_{\mathrm{lv}}\left(A_{3,\mathrm{lv}} - A_{1,\mathrm{lv}}\right),$$

(2)

the work of adhesion associated with E_1 is

$$W_{31} = \gamma_{\mathrm{lv}}(1 + \cos\theta)A_{1,\mathrm{ls}},$$

(3)

the work of adhesion associated with E_2 is

$$W_{32} = \gamma_{\mathrm{lv}}(1 + \cos\theta)A_{2,\mathrm{ls}},$$

(4)

where $A_{1,\mathrm{lv}}$ is the liquid/vapor area in state E_1, $A_{3,\mathrm{lv}}$ is the liquid/vapor area in state E_3, $A_{1,\mathrm{ls}}$ is the liquid/solid area in state E_1 and $A_{2,\mathrm{ls}}$ is the liquid/surface area in state E_2. It is important to note, all energies are calculated as the difference between the final/intermediate state (E_3, E_2) and the initial state (E_1). Thus, excess liquid/vapor energy is a negative quantity, adhesion is a positive quantity and the jumping speed is $v_j = \sqrt{-2E_j/\rho V}$. The initial liquid/vapor and liquid/solid interface areas are given, respectively, by

$$A_{1,\mathrm{lv}} = 4\pi R^2(1 - \cos\theta)$$

(5)

$$A_{1,\mathrm{ls}} = 2\pi R^2 \sin^2\theta.$$

(6)

The other relevant interfacial areas are determined by first considering the total conserved volume of the system based on the two initial droplets of radius R and contact angle θ given by

$$V = \frac{2\pi R^3}{3}(\cos\theta - 1)^2(\cos\theta + 2).$$

(7)

so that the intermediate droplet radius (E_2) is

$$R' = \sqrt[3]{\frac{3V}{\pi(\cos\theta - 1)^2(\cos\theta + 2)}} \, ,$$

(8)

the liquid/vapor and liquid/solid interfacial areas are, respectively,

$$A_{2,\mathrm{lv}} = 2\pi R'^2(1 - \cos\theta),$$

(9)

and

$$A_{2,\mathrm{ls}} = \pi R'^2 \sin^2\theta.$$

(10)

The jumping droplet radius (E_3) is similarly given by considering Eq. (8) as

$$R_\mathrm{j} = \sqrt[3]{\frac{3V}{4\pi}} \, ,$$

(11)

and the jumping droplet liquid/vapor interfacial area is

$$A_{3,\mathrm{lv}} = 4\pi R_\mathrm{j}^2.$$

(12)

It should be noted that we recover the typical two-state expression for the available jumping energy by setting $\eta = 1$ [17,57,58,70]. The efficiency term in Eq. 1 is obtained from our previous study [9] and used under the assumption that the useful internal flow momentum generated during coalescence scales proportionally with the perturbation to the droplet excess surface energy when $\theta < 180°$, which is reasonable when the departure from 180° is small. Note, however, that our previous analysis and resulting expression for η was only valid for Oh ≤ 0.12 in the small Bond number limit, Bo $(= \rho g R^2/\gamma_{\mathrm{lv}}) \to 0$

$$\eta = (3.4026\mathrm{Oh}^2 - 1.5285\mathrm{Oh} + 0.2831)^2\left[3\left(2 - 2^{2/3}\right)\right]^{-1} \quad \text{for} \quad \mathrm{Oh} \leq 0.12.$$

(13)

13

In order to define the efficiency for Oh > 0.12, we assume an exponentially decaying efficiency due to the increasing role of viscous dissipation at large Oh. Such behavior is physically reasonable considering the viscous dissipation behavior observed in our previous simulations [9], but suffers from the fact that the efficiency defined by a simple exponential decay function never goes to zero at a critical Oh, beyond which the bridge formation process is viscously damped and jumping does not occur.. We define this point as corresponding to the droplet size where the viscous-to-inertial cross-over bridge radius, r_c, is equal to the droplet radius, R, which leads to an expression for the critical Ohnesorge number, Oh_c, from the definition of the cross-over timescale and inertial bridge radius scaling [66]

$$Oh_c = D_0^2/8 \tag{14}$$

where D_0 is a constant whose value has been reported to be in the range of 1.39 - 1.62 [66,68,69]. Taking D_0 = 1.62, Eq. (14) predicts $Oh_c \approx 0.33$. For water this corresponds to a critical initial droplet radius that varies from $R_c \approx 400$ nm at 0 °C to $R_c \approx 130$ nm at 20 °C, far smaller than the ~5 μm droplets previously observed experimentally [9].

Next, we fit a double exponential to our previous numerical data and Oh_c (Eq. 14) to obtain an expression for the efficiency

$$\eta = \eta_{max}[e^{-bOh} - (1 - e^{-bOh})e^{-bOh_c}] \text{ for } Oh \le Oh_c, \tag{15}$$

where η_{max} = 0.064 is the maximum efficiency as Oh → 0 (under the constraint of small Bo) and the term in the brackets captures the viscous effect as a function of Oh with a fit parameter, b. Figure 5(a) shows the results of the fit of Eq. (15) with $Oh_c \approx 0.33$ to our previous numerical data [9]. Figure 5(b) shows a comparison of the 3D simulation results of Liu et al. [10] to our efficiency expression, Eq. (15), using the fit parameters given in Figure 6, evaluated in terms of the scaled jumping speed as

14

$$\frac{v_j}{U} = \sqrt{\eta 3(2 - 2^{2/3})}, \tag{16}$$

where $U = \sqrt{\gamma_{lv}/\rho R}$ is the inertial-capillary scaling of the jumping speed [8]. We find good agreement with the full 3D simulation results, importantly capturing the steep reduction in the scaled jumping speed as the jumping droplet radius reduces below ≈ 2 µm.

In the limit of no contact angle hysteresis, we can generate a phase map for jumping as a function of contact angle and Oh. The phase map in Figure 5(c) shows that jumping is not possible for $\theta \lesssim 150°$ for small Oh. Indeed, we calculate that in the limit as Oh → 0 with $\eta_{\mathrm{max}} = 0.064$, the minimum contact angle for jumping is $\theta_{\mathrm{min}} = 147.8°$. We also observe that the critical contact angle for jumping increases as Oh increases up to the no adhesion limit ($\theta = 180°$) where $E_j = 0$ at Oh ≈ Oh_c. The model results are in qualitative agreement with recent 3D lattice Boltzmann simulations [71], showing a similar envelope where jumping is possible. Specifically, there is a steep cut-off in jumping as the apparent contact angle reduces below ~150°. However, our model suggests a larger critical Oh due to our calculated cut-off radius (Eq. (14)). We note that our model suffers from the fact that it cannot implicitly account for external fluid interactions, which may effectively reduce Oh_c [10,71].

To consider the more general case where finite contact angle hysteresis exists, we redefine Eq. (1) as

$$E_j \approx \eta\left[\Delta E_{31,\mathrm{lv}} + (W_{31} - W_{32})\right] + W_{32} + W'. \tag{17}$$

To account for the additional adhesion associated with the pinned regions beneath the droplets, we assume that complete dewetting of the liquid from the structured region is energetically unfavorable compared to some portion of the liquid remaining pinned within the structures on the surface. We can capture this wetting behavior by re-defining the work of adhesion associated

with E_1 as

$$W_{31} = \gamma_{lv}\left[\left(1 + \cos\theta_r^{app}\right)\left(A_{1,ls} - 2A_p\right) + \left[(2 - \varphi) + \varphi\cos\theta_r\right]2A_p\right], \tag{18}$$

where $A_p = \pi r_p^2$ is the pinned area beneath each droplet, θ_r^{app} is the apparent receding angle, θ_r is the receding contact angle on a smooth surface coated with the fluorinated polymer coating ($\approx 112.6°$) and φ is the wetted surface solid fraction associated with the droplet residing in the Cassie-Baxter state. We estimate φ from the advancing apparent contact angle using the Cassie-Baxter equation, $\varphi = \left(\cos\theta_a^{app} + 1\right)/(\cos\theta_a + 1)$. The first term in the brackets of Eq. 18 captures the work of adhesion associated with the wetted area of the surface beyond the pinned base region. Within the second term, the first term in the brackets (2 - φ) represents the creation of new liquid vapor interface between the CNT structures and on the departing droplet. The second term ($\varphi\cos\theta_r$) represents the creation of liquid vapor interface on top of the CNT structures due to droplet surface separation from state 1 to 2. The pinned base radius, r_p, is associated with the initial growth of the condensed droplet nucleating within the CNT nanostructure [40,64] and has been estimated to be ≈ 100 nm for CNT1 based on the results of our previous study [9]. We do not expect the pinned base radius r_p to increase with increasing polymer thickness since the CNT length scale sets this dimension [64]. However, r_p might decrease with increasing polymer thickness due to a slight change in initial growth behavior due to increasing solid fraction [64]. Assuming that r_p is approximately constant for all of our CNT samples, we can estimate the cross-over to constant contact angle growth at the intersection between the r_p dependent contact angle and the macroscopically measured advancing angle. This implies that the switch to constant contact angle growth occurs at smaller droplet radii with decreasing apparent advancing contact angle. Radius-dependent contact angle behavior will continue up to the point where the interface of the droplet makes contact with surrounding

16

nanostructures and begins spreading over the surface in the Cassie state with an approximately constant advancing angle, $\theta_a^{app} \approx 173°$, $163°$, $159°$, and $154°$ for the $\delta = 10$, 30, 60, and 90 nm surfaces, respectively. The early stage variation in the apparent advancing contact angle was modeled as [40,43]:

$$\theta_a^{app}(R) = \cos^{-1}\left(\frac{r_p}{R}\right) + \frac{\pi}{2}.$$ (19)

The droplet radius corresponding to the transition from constant base area growth to constant contact angle growth, R_{cc}, is found by substituting the measured macroscopic apparent advancing contact angle (see Table 1) into Eq. (19) and solving for R to give

$$R_{cc} = \frac{r_p}{\cos\left(\theta_{a,macro}^{app} - \frac{\pi}{2}\right)}.$$ (20)

Figure 6(a) plots the model behaviour of the apparent advancing contact angle for our four CNT surfaces. All surfaces are expected to reach constant contact angle growth mode before their radius reaches 1 μm due to the small pinned base radius. To define the characteristic contact angle hysteresis specific to the surfaces studied here, we fit an expression to the measured contact angle hysteresis. Figure 6(b) plots our experimental $\Delta \cos\theta^{app} = \cos\theta_r^{app} - \cos\theta_a^{app}$ as a function of $1 + \cos\theta_a^{app}$ (see Table 1) and fit the data with

$$\Delta \cos\theta^{app} = m\left(1 + \cos\theta_a^{app}\right)^n.$$ (21)

The work of adhesion associated with E_2 is re-defined as

$$W_{32} = \gamma_{lv}\left(1 + \cos\theta_r^{app}\right)A\left(\theta_a^{app}\right)_{2,ls},$$ (22)

where the wetted area in E_2, $A_{2,ls}$, is defined by the macroscopic apparent advancing angle, θ_a^{app}. The additional work of adhesion term in Eq. (17),

$$W' = \gamma_{lv}\left(\cos\theta_r^{app} - \cos\theta_a^{app}\right)A'_{2,ls},$$ (23)

is defined to capture the additional surface area wetted during the bridge impact process that

17

plays a role in the overall adhesion of the droplet to the surface when the surface wetting behavior is hysteretic. The additional wetted area, $A'_{2,\text{ls}}$, is generated by the inertia of the bridging flow that forces the contact line beyond its equilibrium advancing position. While this dynamically wetted surface area can be inferred and has been observed in previous numerical simulations [12,13], currently little is known quantitatively about this aspect of the coalescence process. Here we consider that $A'_{2,\text{ls}}$ is a function of both the droplet equilibrium advancing angle and Oh. Indeed, as Oh becomes large and the available inertia to drive this dynamic wetting event decreases, we expect $A'_{2,\text{ls}} \to 0$. Thus, we define

$$A'_{2,\text{ls}} = f A_{2,\text{ls}} , \tag{24}$$

where $f(Oh)$ is a factor dependent functionally on Oh. Since $\eta \propto A$, we expect $f(Oh) \propto \eta$ and define

$$f = c[e^{-bOh} - (1 - e^{-bOh})e^{-bOh_c}], \tag{25}$$

where c is a constant that captures the maximum dynamically wetted area in the limit of $Oh \to 0$ and small Bo. We note that re-analysis of available numerical data could help clarify this aspect of the coalescence process [10,12,13,71,72].

To compare our experimental observations to the predictions of Eq. (17), we first set W' = 0 and define a θ_a^{app} dependent contact angle hysteresis based on Eq. 21. Figure 7 shows a phase map generated from Eq. (17) with our experimental observations overlaid. When $E_j > 0$, droplet jumping is not possible and the newly formed droplet remains on the surface (white region in Fig. 7). However, when $E_j < 0$, sufficient excess surface energy is available for conversion into the kinetic energy for droplet jumping, resulting in successful departure (aquamarine shaded region in Fig. 7). For comparison, we have also plotted the prediction of Eq. (17) by considering an idealized surface where no hysteresis exists for the Cassie-Baxter

18

state ($\theta_r = \theta_a$). We see that accounting for hysteresis effects is crucial to explaining the observation of no jumping events for our CNT4 surface, whereas for our CNT1 surface, we can see that the observed jumping threshold ($R_c \approx 556$ nm) is primarily dictated by viscous considerations ($R_c (= 64\mu^2/D_o^4\rho\gamma) \approx 369$ nm) rather than surface adhesion effects as the calculated R_c was 385 nm without hysteresis (~4% increase) and 425 nm when hysteresis behavior was included (~15% increase). This would suggest that further reduction in surface adhesion (larger θ_a^{app}, smaller $\Delta\cos\theta^{app}$) will lead to only small gains in jumping droplet size over what has been demonstrated here.

However, for our CNT2 and CNT3 surfaces, we observe a significant discrepancy between the data and our hysteresis model based on equilibrium interfacial areas ($W' = 0$). The comparison between our model and data can be improved by including an additional adhesion term ($W' > 0$) associated with dynamically (non-equilibrium) wetted surface area driven by the inertia of the bridge impacting the surface during coalescence. The dashed curve in Fig. 7 shows the predictions of our model including an additional dynamically wetted area that is ~10% of the equilibrium wetted surface area in state E_2 in the limit of Oh → 0 and small Bo. Based on this

modification, calculations of the jumping threshold ($E_j = 0$) for the four CNT surfaces yielded minimum initial droplet radii for jumping of 425 nm, 2.05 µm, 14.75 µm and no jumping (Table 2), respectively, in excellent agreement with the experimentally determined values of 530 nm, 3.57 µm, 15.87 µm, and no jumping for $R < 100$ µm. By considering the role of surface adhesion and contact angle hysteresis at different stages of the jumping process in combination with a reasonably bounded viscous dissipation term, we have developed a more physically consistent way of determining the jumping droplet threshold compared to previous estimates [43,60,73]. We expect that as 3D simulations develop to incorporate hysteretic wetting behavior, our

19

understanding can be further refined.

IV. CONCLUSIONS

In summary, we demonstrate for the first time the coalescence-induced jumping of water nanodroplets on superhydrophobic surfaces. The surprisingly small droplet jumping radii we observe reinforces a picture where droplet jumping is governed by capillary-inertial dynamics and fundamentally limited by viscous effects. However, we also demonstrate that, in considering real surfaces, the combined effects of adhesion, contact angle hysteresis and initial wetting behavior governed by the surface structure morphology and length-scale play a defining role. Indeed, it is the coupling of both hydrodynamic and wetting mechanisms that ultimately govern both the minimum droplet jumping size on any given superhydrophobic surface and the reduction in jumping speed at low droplet radii. This work provides key, previously undefined, insights towards designing optimal superhydrophobic structured surfaces for high performance energy and water applications.

REFERENCES

[1]   L. Perez-Lombard, J. Ortiz, and C. Pout, A review on buildings energy consumption information, Energ Buildings **40**, 394 (2008).

[2]   T. B. Peters *et al.*, Design of an Integrated Loop Heat Pipe Air-Cooled Heat Exchanger for High Performance Electronics, Ieee T Comp Pack Man **2**, 1637 (2012).

[3]   A. D. Khawaji, I. K. Kutubkhanah, and J. M. Wie, Advances in seawater desalination technologies, Desalination **221**, 47 (2008).

[4]   J. M. Beer, High efficiency electric power generation: The environmental role, Prog Energ Combust **33**, 107 (2007).

[5]   A. Bürkholz, *Droplet separation* (VCH Verlagsgesellschaft; VCH Publishers, Weinheim (Federal Republic of Germany), New York, NY (USA), 1989).

[6]   E. Schmidt, W. Schurig, and W. Sellschopp, Versuche über die Kondensation von Wasserdampf in Film- und Tropfenform, Forsch. Ingenieurwes **1**, 53 (1930).

[7]   E. J. Le Fevre and J. W. Rose, in *Proceedings of the Third International Heat Transfer Conference* (ASME, Chicago, IL, 1966), pp. 362.

[8]   J. B. Boreyko and C. H. Chen, Self-Propelled Dropwise Condensate on Superhydrophobic Surfaces, Phys Rev Lett **103**, 184501 (2009).

[9]   R. Enright, N. Miljkovic, J. Sprittles, K. Nolan, R. Mitchell, and E. N. Wang, How Coalescing Droplets Jump, ACS Nano **8**, 10352 (2014).

[10]   F. J. Liu, G. Ghigliotti, J. J. Feng, and C. H. Chen, Numerical simulations of self-propelled jumping upon drop coalescence on non-wetting surfaces, J Fluid Mech **752**, 39 (2014).

[11]   F. J. Liu, G. Ghigliotti, J. J. Feng, and C. H. Chen, Self-propelled jumping upon drop coalescence on Leidenfrost surfaces, J Fluid Mech **752**, 22 (2014).

[12]   Y. Nam, H. Kim, and S. Shin, Energy and hydrodynamic analyses of coalescence-induced jumping droplets, Appl Phys Lett **103** (2013).

[13]   Y. Nam, D. Seo, C. Lee, and S. Shin, Droplet coalescence on water repellant surfaces, Soft Matter **11**, 154 (2015).

[14]   X. Chen, J. Wu, R. Ma, M. Hua, N. Koratkar, S. Yao, and Z. Wang, Nanograssed Micropyramidal Architectures for Continuous Dropwise Condensation, Advanced Functional Materials **21**, 4617 (2011).

[15]   J. Feng, Y. Pang, Z. Qin, R. Ma, and S. Yao, Why Condensate Drops Can Spontaneously Move Away on Some Superhydrophobic Surfaces but Not on Others, ACS Applied Materials & Interfaces **4**, 6618−6625 (2012).

[16]   J. Feng, Z. Q. Qin, and S. H. Yao, Factors Affecting the Spontaneous Motion of Condensate Drops on Superhydrophobic Copper Surfaces, Langmuir **28**, 6067 (2012).

[17]   C. J. Lv, P. F. Hao, Z. H. Yao, Y. Song, X. W. Zhang, and F. He, Condensation and jumping relay of droplets on lotus leaf, Appl Phys Lett **103**, 021601 (2013).

[18]   K. Rykaczewski, Microdroplet Growth Mechanism during Water Condensation on Superhydrophobic Surfaces, Langmuir **28**, 7720 (2012).

[19]   K. Rykaczewski, W. A. Osborn, J. Chinn, M. L. Walker, J. H. J. Scott, W. Jones, C. L. Hao, S. H. Yao, and Z. K. Wang, How nanorough is rough enough to make a surface superhydrophobic during water condensation?, Soft Matter **8**, 8786 (2012).

[20]   J. Tian, J. Zhu, H.-Y. Guo, J. Li, X.-Q. Feng, and X. Gao, Efficient Self-Propelling of Small-Scale Condensed Microdrops by Closely Packed ZnO Nanoneedles, The Journal of

Physical Chemistry Letters **5**, 2084 (2014).

[21]   M. McCarthy, K. Gerasopoulos, S. C. Maroo, and A. J. Hart, Materials, Fabrication, and Manufacturing of Micro/Nanostructured Surfaces for Phase-Change Heat Transfer Enhancement, Nanoscale and Microscale Thermophysical Engineering **18**, 288 (2014).

[22]   G. Li, M. H. Alhosani, S. Yuan, H. Liu, A. A. Ghaferi, and T. Zhang, Microscopic Droplet Formation and Energy Transport Analysis of Condensation on Scalable Superhydrophobic Nanostructured Copper Oxide Surfaces, Langmuir **30**, 14498 (2014).

[23]   K. Yanagisawa, M. Sakai, T. Isobe, S. Matsushita, and A. Nakajima, Investigation of droplet jumping on superhydrophobic coatings during dew condensation by the observation from two directions, Applied Surface Science **315**, 212 (2014).

[24]   C.-W. Lo, C.-C. Wang, and M.-C. Lu, Scale Effect on Dropwise Condensation on Superhydrophobic Surfaces, ACS Applied Materials & Interfaces **6**, 14353 (2014).

[25]   K. M. Wisdom, J. A. Watson, X. Qua, F. Liua, G. S. Watson, and C. H. Chen, Self-cleaning of superhydrophobic surfaces by self-propelled jumping condensate, Proceedings of the National Academy of Sciences of the United States of America **110**, 7992 (2013).

[26]   G. S. Watson, L. Schwarzkopf, B. W. Cribb, S. Myhra, M. Gellender, and J. A. Watson, Removal mechanisms of dew via self-propulsion off the gecko skin, J R Soc Interface **12** (2015).

[27]   G. S. Watson, M. Gellender, and J. A. Watson, Self-propulsion of dew drops on lotus leaves: a potential mechanism for self cleaning, Biofouling **30**, 427 (2014).

[28]   J. B. Boreyko, Y. J. Zhao, and C. H. Chen, Planar jumping-drop thermal diodes, Appl Phys Lett **99**, 234105 (2011).

[29]   Q. L. Zhang, M. He, J. Chen, J. J. Wang, Y. L. Song, and L. Jiang, Anti-icing surfaces based on enhanced self-propelled jumping of condensed water microdroplets, Chem Commun **49**, 4516 (2013).

[30]   X. M. Chen, R. Y. Ma, H. B. Zhou, X. F. Zhou, L. F. Che, S. H. Yao, and Z. K. Wang, Activating the Microscale Edge Effect in a Hierarchical Surface for Frosting Suppression and Defrosting Promotion, Sci Rep-Uk **3** (2013).

[31]   J. B. Boreyko and P. C. Collier, Delayed Frost Growth on Jumping-Drop Superhydrophobic Surfaces, Acs Nano **7**, 1618 (2013).

[32]   J. Y. Lv, Y. L. Song, L. Jiang, and J. J. Wang, Bio-Inspired Strategies for Anti-Icing, ACS Nano **8**, 3152 (2014).

[33]   J. B. Boreyko and C. H. Chen, Vapor chambers with jumping-drop liquid return from superhydrophobic condensers, International Journal of Heat and Mass Transfer **61**, 409 (2013).

[34]   D. J. Preston, N. Miljkovic, R. Enright, and E. N. Wang, Jumping Droplet Electrostatic Charging and Effect on Vapor Drag, J Heat Trans-T Asme **136** (2014).

[35]   N. Miljkovic, D. J. Preston, R. Enright, and E. N. Wang, Electrostatic Charging of Jumping Droplets, Nature Communications **4**, 2517 (2013).

[36]   N. Miljkovic, D. J. Preston, R. Enright, and E. N. Wang, Jumping-droplet electrostatic energy harvesting, Appl Phys Lett **105** (2014).

[37]   K. G. Zhang, F. J. Liu, A. J. Williams, X. P. Qu, J. J. Feng, and C. H. Chen, Self-Propelled Droplet Removal from Hydrophobic Fiber-Based Coalescers, Phys Rev Lett **115**, 074502 (2015).

[38]   R. Enright, N. Miljkovic, J. L. Alvarado, K. Kim, and J. W. Rose, Dropwise

Condensation on Micro- and Nanostructured Surfaces, Nanosc Microsc Therm **18**, 223 (2014).

[39] N. Miljkovic and E. N. Wang, Condensation heat transfer on superhydrophobic surfaces, Mrs Bull **38**, 397 (2013).

[40] R. Enright, N. Miljkovic, N. Dou, Y. Nam, and E. N. Wang, Condensation on Superhydrophobic Copper Oxide Nanostructures, J Heat Transf **135**, 091304 (2013).

[41] N. Miljkovic, R. Enright, and E. N. Wang, Effect of droplet morphology on growth dynamics and heat transfer during condensation on superhydrophobic nanostructured surfaces, ACS Nano **6**, 1776 (2012).

[42] N. Miljkovic, R. Enright, and E. N. Wang, Growth Dynamics During Dropwise Condensation on Nanostructured Superhydrophobic Surfaces, 3rd Micro/Nanoscale Heat & Mass Transfer International Conference (2012).

[43] N. Miljkovic, R. Enright, and E. N. Wang, Modeling and Optimization of Superhydrophobic Condensation, J Heat Transf **135** (2013).

[44] J. Cheng, A. Vandadi, and C. L. Chen, Condensation heat transfer on two-tier superhydrophobic surfaces, Appl Phys Lett **101**, 131909 (2012).

[45] E. Olceroglu, C. Y. Hsieh, M. M. Rahman, K. K. S. Lau, and M. McCarthy, Full-Field Dynamic Characterization of Superhydrophobic Condensation on Biotemplated Nanostructured Surfaces, Langmuir **30**, 7556 (2014).

[46] E. Olceroglu, S. M. King, M. M. Rahman, and M. McCarthy, Biotemplated Superhydrophobic Surfaces for Enhanced Dropwise Condensation, Proceedings of the Asme International Mechanical Engineering Congress and Exposition - 2012, Vol 7, Pts a-D, 2809 (2013).

[47] D. Attinger, C. Frankiewicz, A. R. Betz, T. M. Schutzius, R. Ganguly, A. Das, C.-J. Kim, and C. M. Megaridis, Surface engineering for phase change heat transfer: A review, MRS Energy & Sustainability **1** (2014).

[48] X. M. Chen, J. A. Weibel, and S. V. Garimella, Exploiting Microscale Roughness on Hierarchical Superhydrophobic Copper Surfaces for Enhanced Dropwise Condensation, Adv Mater Interfaces **2** (2015).

[49] Y. M. Hou, M. Yu, X. M. Chen, Z. K. Wang, and S. H. Yao, Recurrent Filmwise and Dropwise Condensation on a Beetle Mimetic Surface, ACS Nano **9**, 71 (2015).

[50] N. Miljkovic, R. Enright, Y. Nam, K. Lopez, N. Dou, J. Sack, and E. N. Wang, Jumping-droplet-enhanced condensation on scalable superhydrophobic nanostructured surfaces, Nano Lett **13**, 179 (2013).

[51] P. Birbarah, Z. E. Li, A. Pauls, and N. Miljkovic, A Comprehensive Model of Electric-Field-Enhanced Jumping-Droplet Condensation on Superhydrophobic Surfaces, Langmuir **31**, 7885 (2015).

[52] E. Ölçeroğlu and M. McCarthy, Self-Organization of Microscale Condensate for Delayed Flooding of Nanostructured Superhydrophobic Surfaces, ACS Applied Materials & Interfaces **8**, 5729 (2016).

[53] C.-W. Lo, C.-C. Wang, and M.-C. Lu, Spatial Control of Heterogeneous Nucleation on the Superhydrophobic Nanowire Array, Advanced Functional Materials **24**, 1211 (2014).

[54] K. Rykaczewski, A. T. Paxson, S. Anand, X. Chen, Z. Wang, and K. K. Varanasi, Multimode Multidrop Serial Coalescence Effects during Condensation on Hierarchical Superhydrophobic Surfaces, Langmuir **29**, 881 (2013).

[55] C. Dietz, K. Rykaczewski, A. G. Fedorov, and Y. Joshi, Visualization of droplet departure

on a superhydrophobic surface and implications to heat transfer enhancement during dropwise condensation, Appl Phys Lett **97**, 033104 (2010).

[56] T. Q. Liu, W. Sun, X. Y. Sun, and H. R. Ai, Mechanism study of condensed drops jumping on super-hydrophobic surfaces, Colloid Surface A **414**, 366 (2012).

[57] C. Lv, P. Hao, Z. Yao, and F. Niu, Departure of Condensation Droplets on Superhydrophobic Surfaces, Langmuir **31**, 2414 (2015).

[58] F.-C. Wang, F. Yang, and Y.-P. Zhao, Size effect on the coalescence-induced self-propelled droplet, Appl Phys Lett **98**, 053112 (2011).

[59] X. L. Liu and P. Cheng, 3D multiphase lattice Boltzmann simulations for morphological effects on self-propelled jumping of droplets on textured superhydrophobic surfaces, Int Commun Heat Mass **64**, 7 (2015).

[60] X. L. Liu, P. Cheng, and X. J. Quan, Lattice Boltzmann simulations for self-propelled jumping of droplets after coalescence on a superhydrophobic surface, Int J Heat Mass Tran **73**, 195 (2014).

[61] B. L. Peng, S. F. Wang, Z. Lan, W. Xu, R. F. Wen, and X. H. Ma, Analysis of droplet jumping phenomenon with lattice Boltzmann simulation of droplet coalescence, Appl Phys Lett **102**, 151601 (2013).

[62] Z. Liang and P. Keblinski, Coalescence-induced jumping of nanoscale droplets on super-hydrophobic surfaces, Applied Physics Letters **107** (2015).

[63] See Supplemental Material at http://link.aps.org/ for experimental procedures, and supplemental videos.

[64] R. Enright, N. Miljkovic, A. Al-Obeidi, C. V. Thompson, and E. N. Wang, Condensation on Superhydrophobic Surfaces: The Role of Local Energy Barriers and Structure Length Scale, Langmuir **28**, 14424 (2012).

[65] D. Kaschiev, *Nucleation: Basic Theory With Applications* (Butterworth Heinemann, Oxford, 2000).

[66] J. D. Paulsen, J. C. Burton, and S. R. Nagel, Viscous to Inertial Crossover in Liquid Drop Coalescence, Phys Rev Lett **106**, 114501 (2011).

[67] J. D. Paulsen, J. C. Burton, S. R. Nagel, S. Appathurai, M. T. Harris, and O. A. Basaran, The inexorable resistance of inertia determines the initial regime of drop coalescence, Proceedings of the National Academy of Sciences of the United States of America **109**, 6857 (2012).

[68] S. T. Thoroddsen, K. Takehara, and T. G. Etoh, The coalescence speed of a pendent and a sessile drop, Journal of Fluid Mechanics **527**, 85 (2005).

[69] M. M. Wu, T. Cubaud, and C. M. Ho, Scaling law in liquid drop coalescence driven by surface tension, Phys Fluids **16**, 51 (2004).

[70] M. Kollera and U. Grigull, The bouncing off phenomenon of droplets with condensation of mercury, Wärme - und Stoffübertragung **2**, 31 (1969).

[71] S. Farokhirad, J. F. Morris, and T. Lee, Coalescence-induced jumping of droplet: Inertia and viscosity effects, Phys Fluids **27**, 102102 (2015).

[72] Y. Cheng, J. Xu, and Y. Sui, Numerical investigation of coalescence-induced droplet jumping on superhydrophobic surfaces for efficient dropwise condensation heat transfer, International Journal of Heat and Mass Transfer **95**, 506 (2016).

[73] M. He *et al.*, Hierarchically structured porous aluminum surfaces for high-efficient removal of condensed water, Soft Matter **8**, 6680 (2012).

[74] M.-K. Kim, H. Cha, P. Birbarah, S. Chavan, C. Zhong, Y. Xu, and N. Miljkovic,

Enhanced Jumping-Droplet Departure, Langmuir **31**, 13452 (2015).
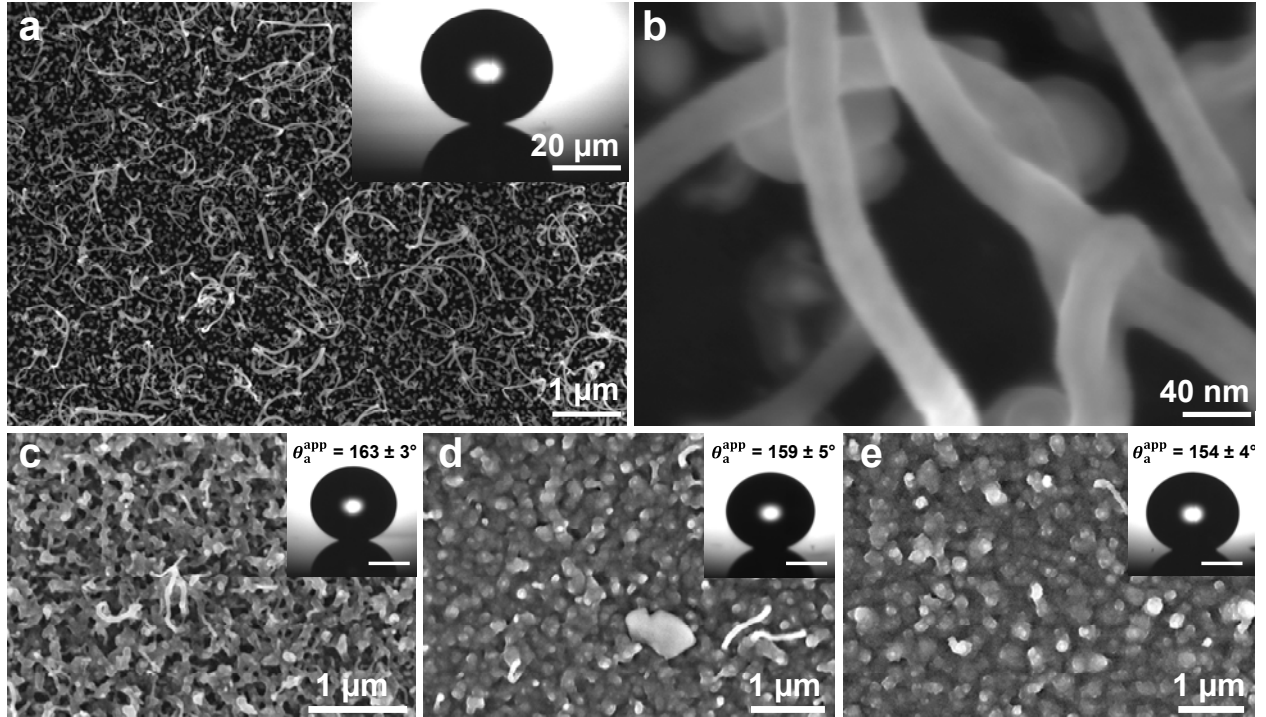
FIGURES

Figure 1. Field emission scanning electron micrographs (Hitachi model S-4800) of (a) a top-down view of the CNT surface coated with a ≈10 nm thick layer of P2i fluoropolymer (CNT1) and (b) a high magnification view of individual CNTs shown in (a). Inset: Microscopic droplet in the receding state on the P2i-coated CNT surface (θ_r^{app} = 164 ± 6°). The CNTs have characteristic diameters $d \approx$ 7 nm, heights, $h \approx 1$ μm, and solid fraction, $\varphi \approx 0.017$. Field emission scanning electron micrographs of a top-down view of the (c) CNT2, (d) CNT3, and (e) CNT4 surfaces coated with 30 nm, 60 nm, and 90 nm thick layers of P2i fluoropolymer, respectively. Insets: Microscopic droplets in the advancing state on the P2i-coated CNT surfaces. Inset scale bars are 20 μm each. The effective solid fraction of the CNT surfaces shown in (c), (d), and (e) are estimated as $\varphi \approx 0.06$, 0.15, and 0.23, respectively.
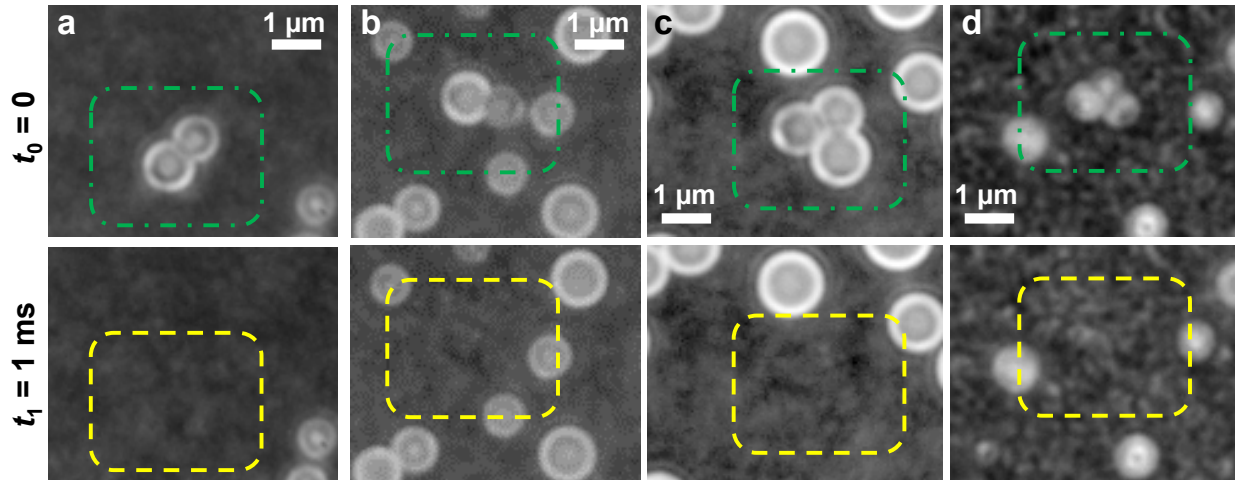
Figure 2. Time-lapse images captured via top-view optical microscopy of steady state water condensation on the superhydrophobic CNT1 surface. Condensing nanoscale droplets having (a) $R_1 = 685 \pm 75$ nm (bottom) and $R_2 = 640 \pm 75$ nm (top), (b) $R_1 = 792 \pm 75$ nm (left) and $R_2 = 533 \pm 75$ nm (right), (c) $R_1 = 762 \pm 75$ nm, $R_2 = 716 \pm 75$ nm, and $R_3 = 792 \pm 75$ nm, and (d) $R_1 = 727 \pm 75$ nm, $R_2 = 681 \pm 75$ nm, and $R_3 = 568 \pm 75$ nm, underwent spontaneous jumping after coalescence. Green dot-dash squares highlight areas of the surface just prior to coalescence, while yellow dashed squares highlight areas of the surface immediately after jumping (1 ms later). High speed imaging was done at 1,000 frames/s, with an exposure time of 200 μs, and a period of 1 ms. See also Video S1 in the Supplemental Material [63]. An imaging frame rate of 1,000 frames/s was chosen to maximize the capture screen resolution and hence number of coalescence events, and to provide a high enough temporal resolution to ensure that returning droplets do not trigger coalescence and jumping [74].
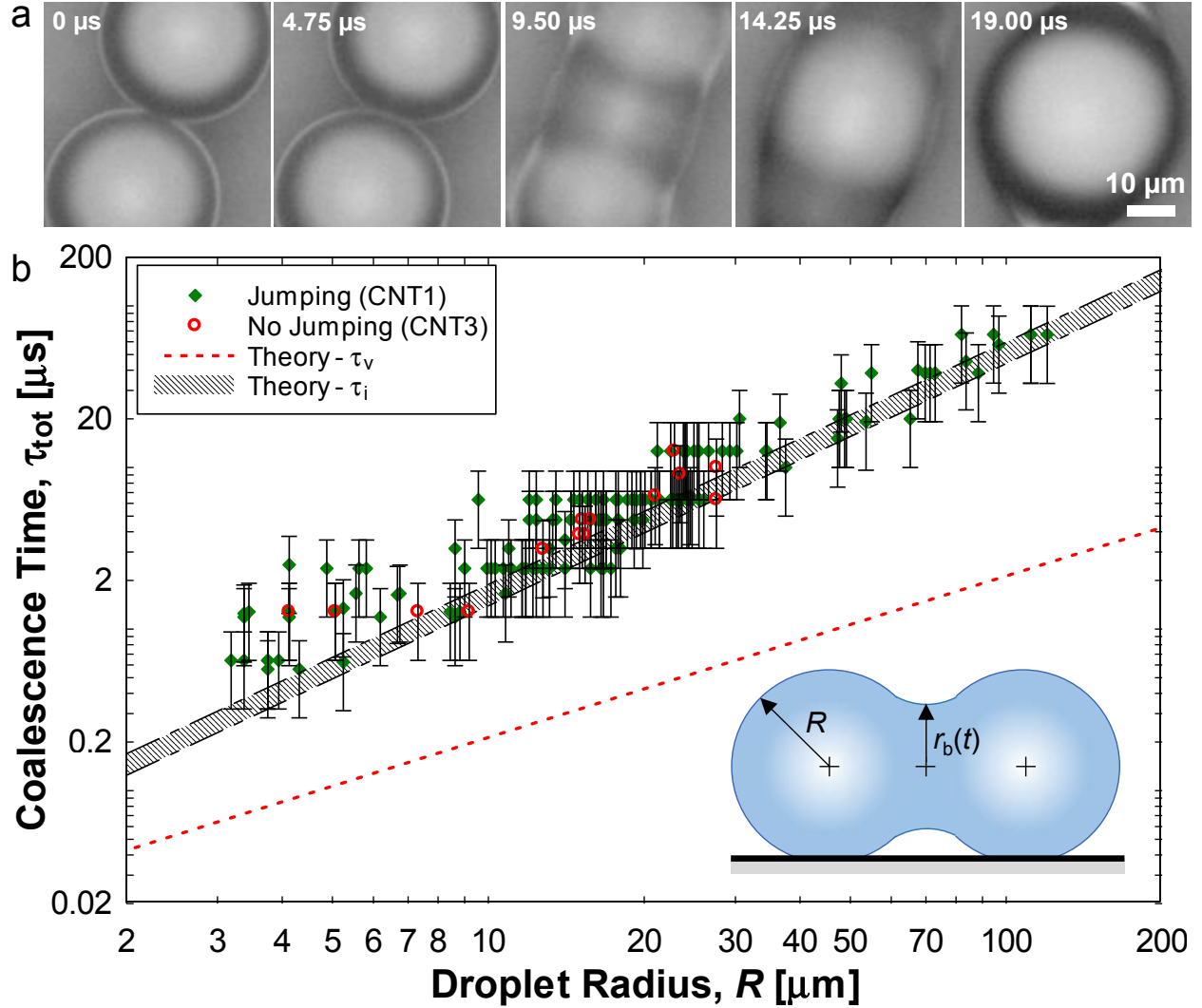
Figure 3. (a) High-speed time-lapse images capturing the coalescence process of two identical (R_1 = 18.5 ± 0.3 μm (bottom) and R_2 = 18.5 ± 0.3 μm (top)) water droplets via top-view optical microscopy. Droplet were formed by condensing water vapor from the ambient air. Experimental conditions: stage and CNT sample temperature T_w = 1 ± 0.5°C, ambient air temperature T_{air} = 22 ± 0.5°C, vapor temperature $T_v = T_{sat}(\Phi P_{sat}(T_{air}))$ = 2.5 ± 0.5°C, relative humidity Φ = 28 ± 1%, and supersaturation $S = [\Phi P_{sat}(T_{air})]/P_{sat}(T_w)$ = 1.02 ± 0.035. High speed imaging was done at 210,526 frames/s, with an exposure time of 4.75 μs, and a period of 4.396 μs. (b) Two droplet coalescence time (τ_{tot}) as a function of initial droplet radius, R. The coalescence time is defined as the time taken for the bridge radius to reach the in-plane droplet radius ($r_b = R$, see inset schematic). The filled green diamond and hollow red circle symbols represent experimentally observed jumping events on CNT1 and coalescence without jumping on CNT3, respectively. For inertial-capillary dominated coalescence: $\tau_{tot} = (\rho R^3/\gamma D_0^4)^{1/2}$. The shaded region represent the solution for $1.39 < D_0 < 1.62$. For inertially-limited viscous coalescence: $\tau_{tot} = R\mu/\gamma$. The error bars for the measured radii are smaller than the symbol size and are not shown. See also Videos S2 and S3 in the Supplemental Material [63].
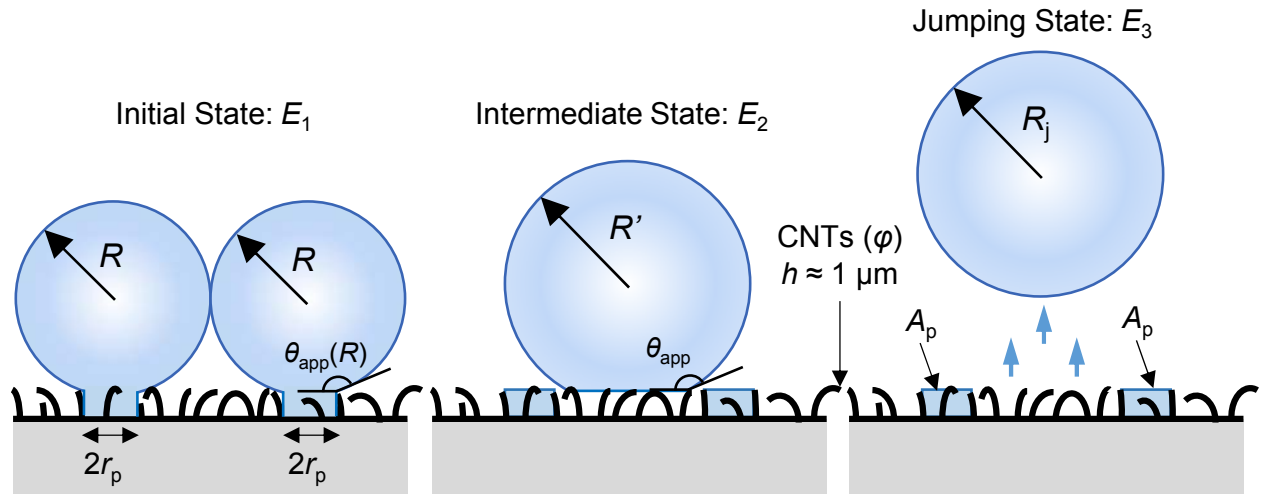
Figure 4. Schematic of droplets residing in state 1 (E_1) just prior to jumping, state 2 (E_2) after coalescing but before departing, and state 3 (E_3) immediately after jumping. In addition to the initial state before coalescence (E_1) and the final jumping state (E_3), we consider an intermediate state representing the coalesced droplet on the surface prior to departure (E_2). The intermediate state (E_2) is a well-defined equilibrium state if jumping does not occur.
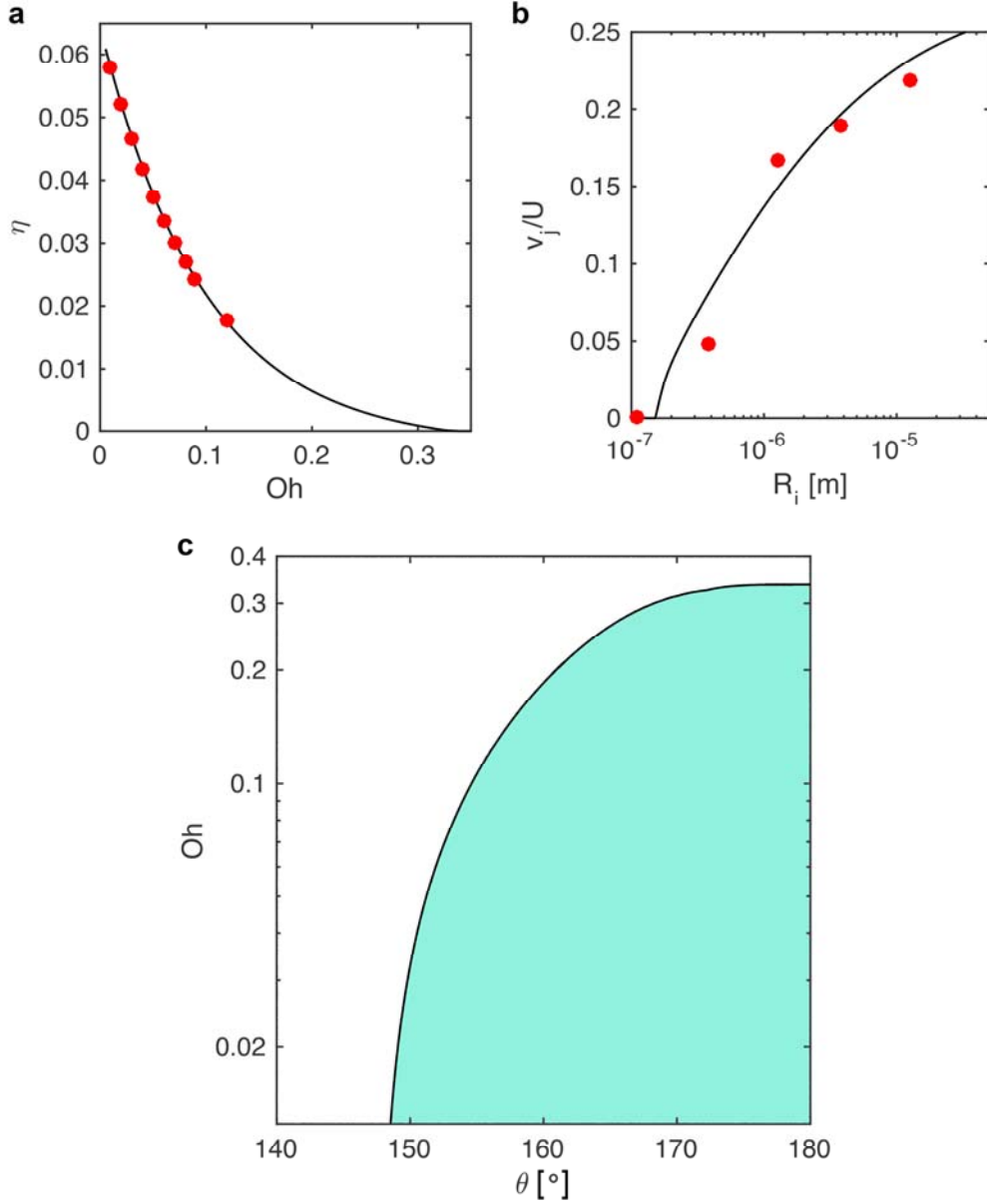
Figure 5. Energy conversion efficiency & idealized surface jumping droplet phase map. (a) Fit of Eq. (15) to numerical data to obtain η for $Oh \leq Oh_c$ in the limit of small Bo. A best fit of Eq. (15) to the numerical data (red circles) [9] with $Oh_c = 0.32805$ gives $\eta_{max} = 0.064362$ and $b = 10.165$. The Pearson product moment of the fit is $R^2 = 0.99948$. (b) Comparison of the exponentially decaying jumping efficiency expression (Eq. (16), solid curve) to the 3D numerical results of Liu et al. [10] (red circles) in terms of the scaled jumping speed versus droplet jumping radius (R_j). Properties taken from the NIST Standard Reference Database corresponding to water at 20°C. (c) Jumping droplet phase map in terms of Oh and contact angle (θ) for the idealized case where the jumping surface demonstrates zero contact angle hysteresis. In the right-hand side shaded region bounded by the $E_j = 0$ contour, Eq. (1) predicts jumping is possible ($E_j < 0$), while

in the left-hand side un-shaded region bounded by the $E_j = 0$ contour, $E_j > 0$ such that jumping is not possible.
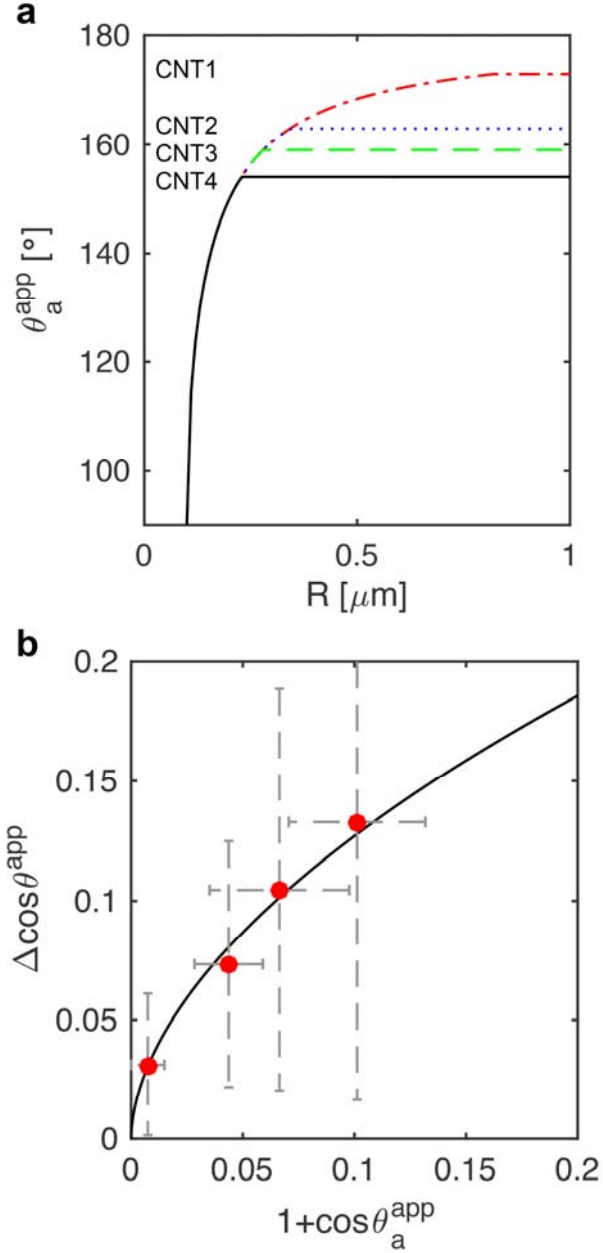
Figure 6. CNT surface wetting characteristics. (a) Apparent advancing contact angle model. The apparent contact angle varies with droplet radius given by Eq. (19) from a pinned base radius of $r_p = 100$ nm that is assumed constant for the four CNT surfaces. The transition to constant contact angle growth given by Eq. (20) occurs when the advancing contact angle equals the macroscopically measured value. (b) Contact angle hysteresis model. Fit of Eq. (21) to the experimental contact angle data to obtain contact angle hysteresis for $\theta_a^{app} \leq 180°$. A best fit of Eq. (21) to the numerical data gives $m = 0.4497$ and $n = 0.5492$. The Pearson product moment of the fit is $R^2 = 0.9902$.
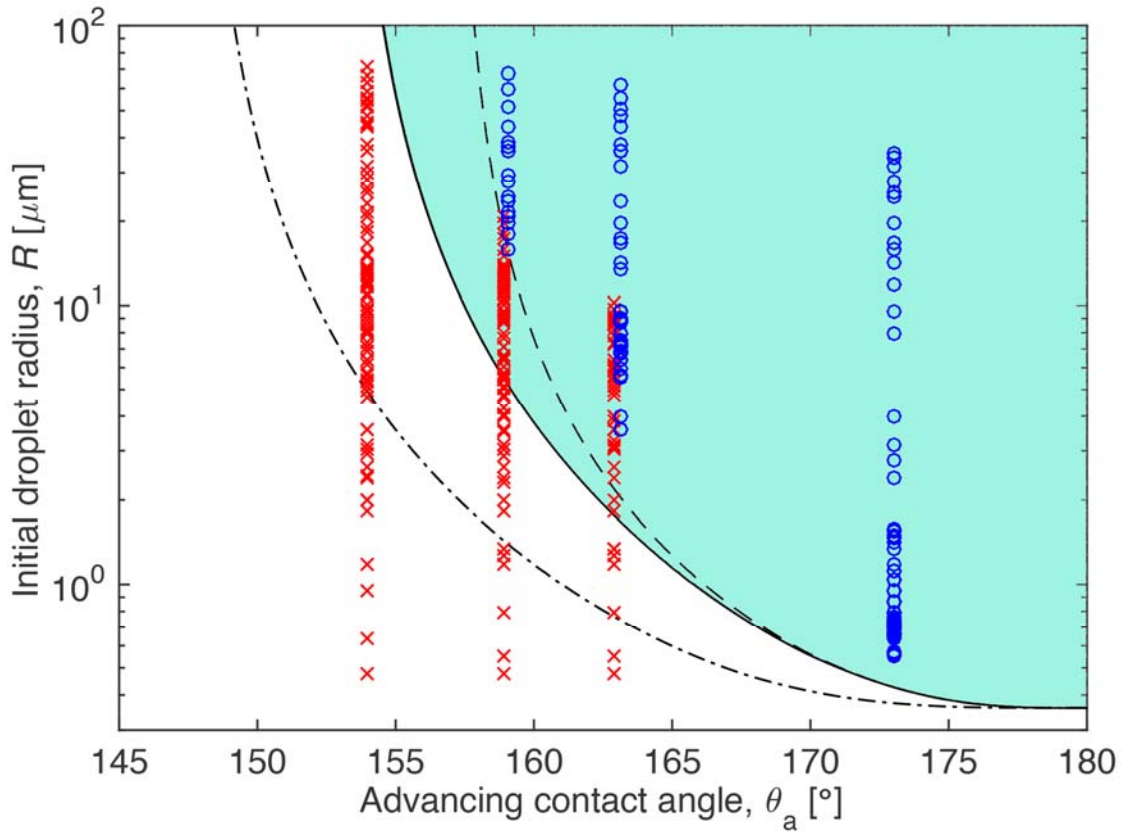
Figure 7. Regime map of droplet jumping showing the initial droplet radius (R) as a function of advancing contact angle. The blue circle and red cross symbols represent experimentally observed jumping events and coalescence without jumping, respectively. The solid curve gives the model prediction with hysteresis considering the equilibrium interfacial areas (see Fig. 4) with $r_p = 100$ nm. The shaded region represents the regime where droplet jumping is allowable ($E_j < 0$), while the un-shaded region represents the regime where droplet jumping does not occur ($E_j > 0$). For comparison, we plot the no hysteresis limit (dot-dash curve). Also shown (dashed curve) is the prediction of the hysteresis model including an additional Oh-dependent adhesion term W' ($c = 0.11$) accounting for the dynamically wetted area between states E_2 and E_3. Note, the experimental data points are offset to the left and right, respectively, for the CNT2 and CNT3 samples to more clearly show the data. Experimental conditions: $S = 8.56 \pm 0.4$, $T_w = 1 \pm 0.5°C$.

Table 1. Surface parameters, measured contact angles, and critical jumping radii used in fitting the jumping model with hysteresis.

Sample	t_{P2i}	$\theta_{a,app}$	$\theta_{r,app}$	φ	$R_c = R_j/2^{1/3}$ (experiment)
P2i	10 nm	124.3	112.6	NA	NA
CNT 1	10nm	173°± 3.5°	164°± 6°	~0.017	556 ± 75 nm
CNT 2	30 nm	163°± 3°	152°± 6°	~0.059	3.57 ± 0.075 μm
CNT 3	60 nm	159°± 5°	146°± 8°	~0.152	15.87 ± 0.075 μm
CNT 4	90 nm	154°± 4°	140°± 10°	~0.232	Not observed

Table 2. Surface parameters used in fitting the jumping model with hysteresis and calculated critical jumping radius.

Sample	c	$\theta_{a,app}$	$\theta_{r,app}$[i]	φ	R_c (theory)
CNT 1	0.11	173°	164.1°	~0.017	425 nm
CNT 2	-	163°	151.1°	~0.059	2.05 μm
CNT 3	-	159°	146.3°	~0.152	14.75 μm
CNT 4	-	154°	140.4°	~0.232	No jumping predicted

[i] Based on fit to data, Eq. (21)